remote sensing

MDPI

Article

Tectonism of Late Noachian Mars: Surface Signatures from the Southern Highlands

Trishit Ruj [1,*], Goro Komatsu [2], Gene Schmidt [3], Suniti Karunatillake [4] and Kenji Kawai [5]

[1] Institute of Space and Astronautical Science (ISAS), Japan Aerospace Exploration Agency (JAXA), 3-1-1 Yoshinodai, Sagamihara 252-5210, Kanagawa, Japan
[2] International Research School of Planetary Sciences, Università d'Annunzio, Viale Pindaro 42, 65127 Pescara, Italy
[3] Department of Science, Università Degli Studi Roma Tre, 00154 Rome, Italy
[4] Department of Geology and Geophysics, Louisiana State University, Baton Rouge, LA 70803, USA
[5] Department of Earth and Planetary Science, School of Science, University of Tokyo, Hongo 7-3-1, Tokyo 113-0033, Bunkyo, Japan
* Correspondence: trishitruj@gmail.com or ruj.trishit@jaxa.jp

Abstract: Upwelling mantle plumes often instigate extensional stress within the continental crust of Earth. When stress exceeds crustal strength, extensional structures develop, reducing the effective stress and trigger magmatic processes at the crust–mantle boundary. However, such processes and their relationship to the formation of many surface structures remain poorly characterized on Mars. We identified a series of extensional structures in the southern highlands of Mars which collectively resemble continental rift zones on Earth. We further characterized these extensional structures and their surrounding region (area of ~1.8 M km^2) by determining the surface mineralogy and bulk regional geochemistry of the terrain. In turn, this constrains their formation and yields a framework for their comparison with extensional structures on Earth. These terrains are notable for olivine and high-Ca pyroxene with a high abundance of potassium and calcium akin to alkali basalts. In the case of Mars, this Earth-like proto-plate tectonic scenario may be related to the plume-induced crustal stretching and considering their distribution and temporal relationship with the Hellas basin, we conclude that the plume is impact-induced. Overall, the findings of this work support the presence of mantle plume activity in the Noachian, as suggested by thermal evolution models of Mars.

Keywords: Mars tectonics; extensional tectonics; plume-induced crustal stretching; Noachis Terra; Circum Hellas volcanism; Hellas impact

Citation: Ruj, T.; Komatsu, G.; Schmidt, G.; Karunatillake, S.; Kawai, K. Tectonism of Late Noachian Mars: Surface Signatures from the Southern Highlands. *Remote Sens.* **2022**, *14*, 5664. https://doi.org/10.3390/rs14225664

Academic Editor: Giancarlo Bellucci

Received: 22 September 2022
Accepted: 7 November 2022
Published: 9 November 2022

1. Introduction

The internal dynamics [1,2] of terrestrial planets have contributed tremendously to the evolution of their outer surfaces. Mars, with low present-day heat flow (avg. 19 mWm^{-2}; [3]), may have lost most of its internal heat by generating superplumes [4] at the very early phase of evolution through volcanism and tectonism [5], perhaps in a form of heat-pipe processes [2,6]. It is well accepted that early Mars possessed a periodically reversing Earth-like magnetic field (thermoremanent magnetization in first ~500 Ma to ~800 Ma; [7–9] since its formation), which possibly resulted due to surface heat flux enhanced by plate tectonics [10]. There are compelling indications of the existence of transform faults [8] and arguments that the northern lowlands formed due to seafloor spreading [11]. On a regional scale, several extension zones in and around Tharsis have been characterized by the 'planetary analogs to terrestrial continental rifts' [12–14] with additional support from giant impacts [13]. However, typical Earth-like plate tectonics models for Mars have been strongly criticized in the absence of any notable present-day plate boundaries on the surface [15]. According to Breuer and Spohn (2003) [16], early Mars plate

tectonics models become difficult to reconstruct with a post-plate tectonics crust; however, they do not exclude the possibility of an "early phase of plate tectonics" that was unable to develop fully. In the southern highlands, especially in the Noachis Terra and Terra Sabaea regions, we found evidence of volcanoes and volcanic resurfacing associated with tectonic fabrics. These tectonic fabrics include extensional structures of diverse architecture and morphology (Figure 1A) such as grabens, half grabens, and transfer faults. Such arrangement of structures and the associated rocks can reveal the dynamic evolution of terrestrial planets.

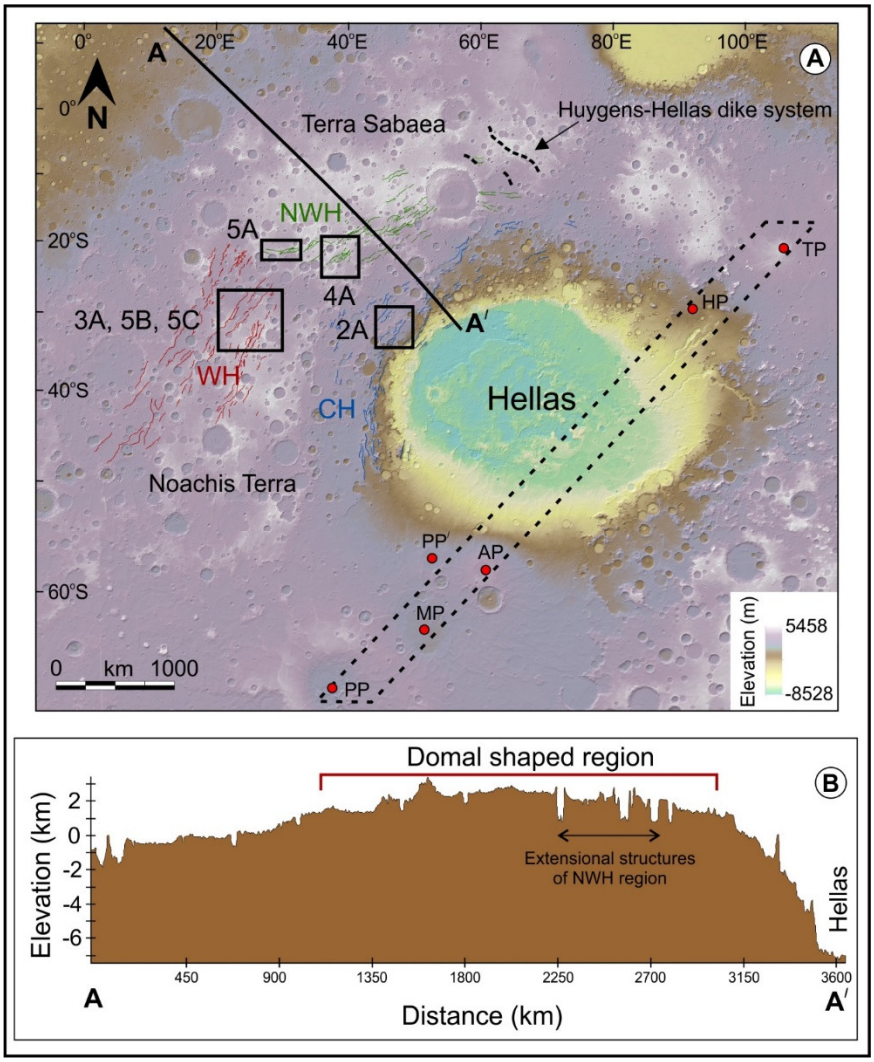

Figure 1. (**A**) Colorized elevation map showing the distribution of extensional structures around the Hellas basin. The red dots indicate the positions of Paterae associated with volcanism. CH: Circum Hellas structures (marked in blue lines); WH: Western Hellas (structures marked in red lines), NWH: North-western Hellas (structures marked in green lines); dashed parallelogram represents the linear orientation of Paterae in the Circum Hellas Volcanic Province (CHVP). A topographic profile transect (AA') is shown in (**B**). AA' shows the extensional structures on the top of the domal (~2 km) region. (PP: Pityusa Patera; MP: Malea Patera; PP': Peneus Patera; AP: Amphitrites Patera; HP: Hadriaca Patera; TP: Tyrrhena Patera).

On Mars, an abundance of orbital spectroscopy has been focused on possible extensional features [17–19] which show basaltic material consisting of feldspar, high and low-calcium pyroxene, and higher olivine enrichment than the surroundings. These settings have been proposed to have originated in volcano-tectonic settings. However, a debate is ongoing about whether many features on the surface of Mars are extensional or form from vertical collapse, including both small-scale graben [17,20,21] and areas associated with

Tharsis [22–24] and the Hellas impact [23–25]. On Earth, areas of rifting are usually associated with alkaline volcanic rocks, which makes concentrations of sodium and potassium unique markers for extensional settings on Mars.

Previous hypotheses suggest that the Martian extensional structures around Tharsis were produced by concentric extensional membrane stresses [26]. On the other hand, Hellas basin concentric structures were modeled as a product of the Hellas basin's isostatic relaxation [27] and basinward drag of the upper lithosphere [23]. These late Noachian-aged extensional structures [28] were categorized as the result of the upper lithosphere's drag [23] towards the interior of the Hellas basin without much consideration of the morphological and petrological observations. To clarify the origin of the tectonic structures around the Hellas basin, we assessed the morphology and geometry of tectonic structures from the study area using ConTeXt (CTX) [29] and High-Resolution Stereo Camera (HRSC) images [30,31]. To subsequently interpret early Martian geologic evolution and the consistency between the lithology and tectonic structures, we consider the mineralogy derived from the Compact Reconnaissance Imaging Spectrometer (CRISM) hyperspectral data [32] and regional bulk geochemistry from the Gamma Ray Spectrometer (GRS) data [33]. Evaluating the results, we hypothesize an uprising mantle plume [1] responsible for the extensional structures in the Noachis–Sabaea region. These findings contribute to the understanding of the Martian heat loss mechanism and the generation of tectonic structures that formed in and around the same time (3.8 Ga) or before the earliest paleomagnetic evidence of plate motion on Earth. Furthermore, investigation of the tectonic structures further constrains the mystery of the absence of plate boundaries on Mars and its effect on the volcano-tectonic evolution of the planet.

2. Geology of the Study Area

The study area is located within the Noachis Terra and Terra Sabaea regions which are part of the southern highlands of Mars (Figure 1A). The latter region is heavily resurfaced by giant impact craters, such as Hellas, Argyre, Huygens, and Isidis, as well as their impact ejecta deposits [15,34]. It also consists of Pre-Noachian to Hesperian-aged volcanic plains (Hesperia Planum, Syrtis Major Planum) [35] surrounded by the Noachian massive highland units [15,25]. As a key source/pathway of lava to the volcanic plains (i.e., feeder), giant dikes (Figure 1A) are reported from the northern part of the Hellas basin [36]. Hesperian compressional tectonics are recorded within the volcanic plains as wrinkle ridges [28,37–39]. The orientations of these compressional structures indicate ENE-WSW compressive stress responsible for their formation, and the timing coincided with the Martian global peak contraction [38–40]. The late Noachian-aged extensional structures [28] are mostly concentrated around the western and northern parts of the Hellas basin, in between the Hellas and Argyre basins (Figure 1B). The responsible stresses for these extensional structures were previously linked to the development of the Hellas basin [18,23]. The eastern part of the Hellas basin has been identified with the presence of volcanoes and their associated Paterae (red dots in Figure 1A) of the late Noachian period [19,24]. According to Williams et al., (2009) [24], morphologically, they resemble flood volcanism from localized edifice-building eruptions. Strong positive gravity anomalies indicate the possibility of dense magma bodies beneath these volcanoes [24].

The Hellas impact and its perimeter areas have been studied extensively through spectral analyses. Irwin et al. (2018) [41] detected a wide variety of minerals (e.g., olivine, pyroxene, feldspar, phyllosilicates, sulfates, and chlorite) in the area of Terra Sabaea, north–northwest of the Hellas impact perimeter. Though the work focused primarily on crater floors, areas within some of the Hellas-concentric graben were considered to have contained lava flows, whereas felsic materials within craters was concluded as of basement rocks. The Hellas basin itself contains an abundance of lava flow and basaltic material, as well as many types of sedimentary and volcanic deposits that have undergone extensive aqueous alteration [42–44]. Due to its complicated geologic history, bedrock is often covered and not always detectable within higher-resolution CRISM observations.

However, Thermal Emission Spectrometer (TES) and Mars Express Observatoire pour la Minéralogie, l'Eau, les Glaces, et l'Activité (OMEGA) instruments are useful in analyzing the general mineralogy of larger areas, in which regional transitions from high-calcium pyroxene poor to high-calcium pyroxene rich can be observed across the outer rings of the Hellas impact basin [45]. The CHVP shows a complicated composition of volcanic material, which is difficult to discern but potentially consists of tuff, basaltic lava flows, or a combination of the two [24]. Furthermore, attempts have been made to place an epicenter of volcanism on the eastern side of the CHVP [46] based on the possible identification of volcanic edifices (e.g., calderas) and outflow channels that lead into Hellas basin. In this research, we tried to explore the possibilities of the genetic links between CHVP and the extensional structures in the study area.

3. Methodology

We utilized a variety of orbital data sets to distinguish the characteristics of the linear structures observed around the Hellas basin. Here, we also used the previously published morpho-structural maps [15,25] and reevaluated them using CTX camera images (6 m/pixel) [29] and HRSC-Mars Orbital Laser Altimeter (MOLA) blended Digital Elevation Models (DEM) (200 m/pixel) [47] to discriminate and categorize each of characteristic structures. The mineralogy of the associated lithology was inferred from CRISM data and further validated with available terrestrial spectra from the USGS library for the reliable determination of the mineral type [48]. We used seven full-resolution observations (FRT, 18 m/pixel) and four half-resolution observations (HRL, 36 m/pixel) from relatively dust-free regions of the grabens and the associated region. We used the CRISM Analysis Tool (CAT) package available in the Environment for the Visualization of Images (ENVI), following the method described by Flahaut et al. (2015) [49] and Schmidt et al. (2022) [50]. Both the photometric correction and volcano-scan atmospheric correction methods available in CAT were used in all the presented ratioed spectra. CRISM analysis was focused primarily on spectral features in the near-infrared but also the visible spectrum when specifically determining the presence of olivine. Spectral parameters from Viviano-Beck et al. (2014) [51] were used to map absorptions specific to certain minerals. In some areas, hydrated minerals were identified by observing the overtones and fundamental vibrational absorption features in the 1.0–2.6 μm interval, where CRISM can identify hydrated minerals [49,52]. We examined individual pixels for relevant signatures and created regions of interest (ROI) with averages of 10 pixels. Spectral parameters from band depth calculations at relevant wavelengths were mapped to identify the presence of a given mineral. The key parameters used were OLINDEX3, LCPINDEX2, HCPINDEX2, and BD1300 [51,53]. We complemented these local outcrop scale characterizations with the bulk (i.e., decimeter depth scales) regional geochemistry derived from GRS data [54] within the study area. To determine the geochemical signatures of geologic evolution, here, we compared the regional geochemistry to the rest of the Martian crust (i.e., the Martian crust in the mid to low latitudes, excluding the study region as a means of minimizing sampling biases) following a modified box plot method [55]. We analyzed four GRS-derived chemical maps (Ca, K, Si, and Th) from the Planetary Data System and the public archive [54] of published papers. In our analysis, we excluded polar regions from the analysis to reduce the effects of elevated hydrogen, limiting the chemical maps to 5° × 5°-pixel resolution in the mid-latitudes.

We integrated the data into the ArcGIS platform (version 10.8.1) using a Lambert Conformal Conic projection.

4. Results

4.1. Morpho-Structural Features

The extensional structures (marked in red, blue, and green; Figure 1A) are mostly distributed on the western boundaries of the Hellas basin, following the outer ring curvature of the Hellas basin or at a high angle to it [28]. These structures were categorized according to their distributions around the Hellas basin as (a) Circum Hellas (CH), (b) Western Hellas (WH), and (c) North-western Hellas (NWH). The extensional structures of the CH region are in close proximity to the Hellas basin (Figure 2A), most common in the western boundaries, and extend to the northwestern and northern margins. The extensional zone from this set of structures is defined with a series of concentric normal faults dipping towards the Hellas basin, and grabens are tilted basinward (Figure 2B) (set 1 graben on Figure 2: [25]). The extracted profile sections (Figure 2B) suggest that the graben shoulder away from the basin is always at a higher elevation than the shoulder nearer to the basin. The average widths of the grabens are ~35 km with a maximum arc length of 200 km [25]. On the other hand, WH and NWH extensional structures do not show any trend to follow the curvature of the Hellas basin rim and are at a high angle to it. In contrast to the CH extensional structures, the elevation profiles of the WH and NWH grabens rule out the possibility of shoulder elevation offsets in the graben bounding normal faults, and tilt in the graben floor is also missing. The WH grabens are the widest (maximum width > 100 km) and lengthiest (maximum length of 1200 km) among all other sets of extensional structures. WH extensional structures generally trend in the NNE-SSW direction (Figure 3A–C). In the case of NWH extensional structures (Figure 4A–C), they extend ~1500 km, with an ENE-WSW trend, and the average graben width is ~30 km. The maximum width of the WH and the NWH extension zones are 700 and 150 km, respectively.

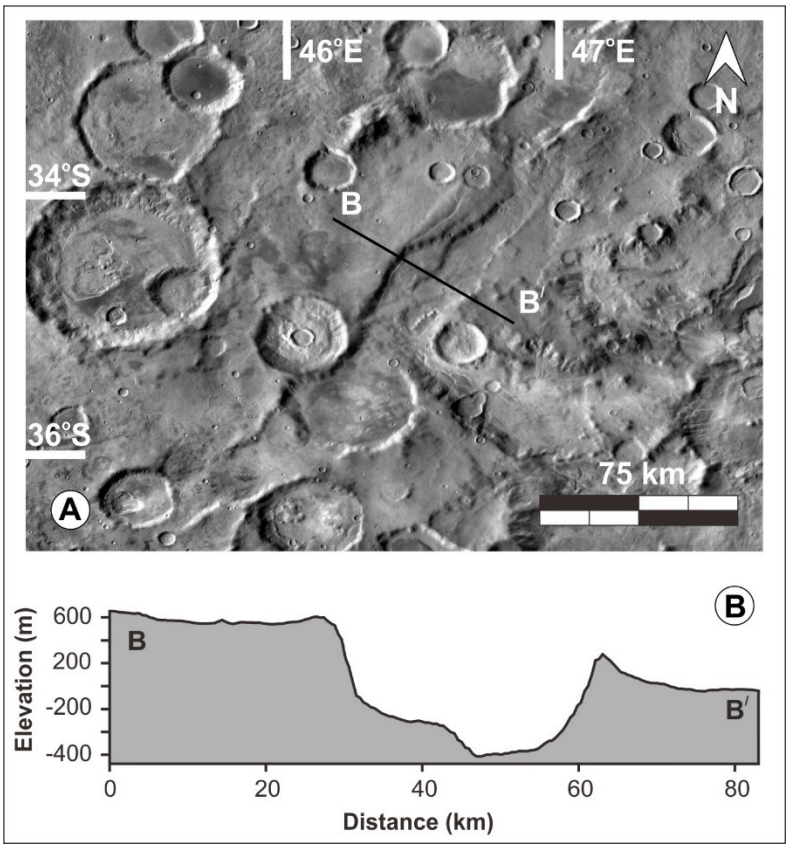

Figure 2. (**A**) CH extensional structures are shown in THEMIS images in the western flank of the Hellas basin. (**B**) A topographic profile section is extracted along B–B′ using HRSC−MOLA blended DEM. The derived profile section clearly shows the difference in elevation on each side of the graben.

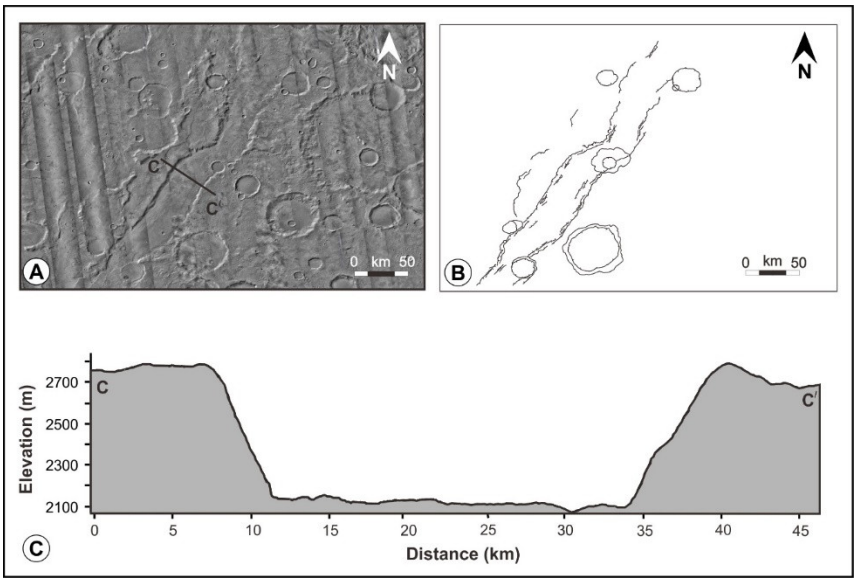

Figure 3. (**A**) WH extensional structures shown on CTX images. High-resolution view of a 35 km wide WH graben in Noachis Terra region. (**B**) Traces of structures drawn over Figure A. (**C**) the topographic profile section C–C′ shows that the graben in this set of extensional structures have similar elevations implying both faults on either side of the graben have received equal importance during extension.

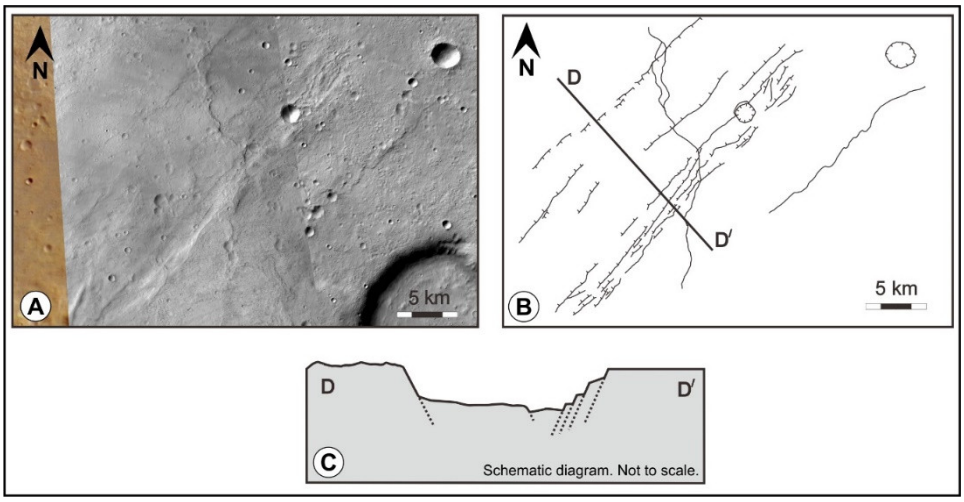

Figure 4. (**A**) NWH extensional structures are shown in the CTX image with its central location 27°55′E/28°15′S. (**B**) High-resolution view of a 10 km wide NWHG. Detailed structures are drawn over Figure A. (**C**) graphical representation of the topographic profile section D–D′.

Extracted HRSC-MOLA blended DEMs around the WH and NWH regions portray a domal shape of the basement along the WH and NWH regions. The domal region is ~2 km higher than the surroundings (Figure 1B). The dominant extensional structures among these two sets (WH and NWH) include grabens, collateral synthetic faults (Figure 5A), and relay ramps. Grabens typically have the elevation offset of the bounding normal faults between 0.8 and 1.0 km. Collateral synthetic faults of the NWH region form a succession half-graben with a crescent-shaped geometry, where one half-graben ends, and typically the next one takes over. Relay structures and ramps (Figure 5B–D) form in the process of strain transformation from one fault to another [56]. These first-order relay structures are typical of accommodation zones observed in all active terrestrial rift zones, including the Rio Grande and East African Rift systems [57]. However, we do not observe matured rift zones surface features such as transfer faults (resulting due to rift perpendicular shearing; [57]) and isolated volcanic edifices (inferring plate opening is accommodated by faulting;

[58]) along the rift valley (in both cases, WH and NWH region). Instead, fissure eruptions dominate along the faults in the WH and NWH regions. It should be noted that we found low, narrow, and broadly arcuate giant dikes of the late Noachian age [36] in the eastern part of the NWH region.

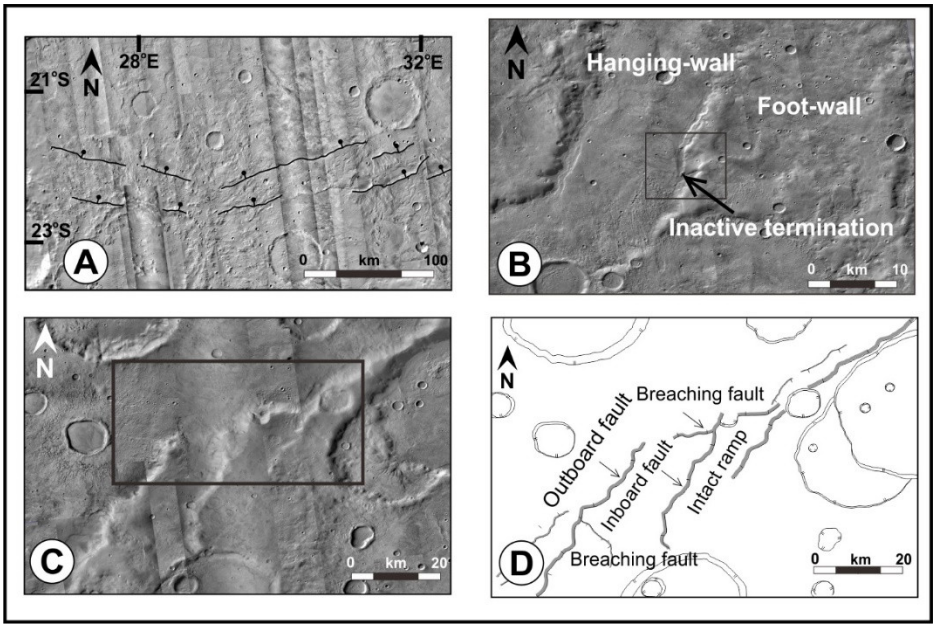

Figure 5. (**A**) A magnified region showing collateral synthetic half grabens with half-moon-shaped geometry. Balls indicate downdip direction. (**B**) Relay ramps associated with the graben. (**C**) Relay structures associated with a half-graben. Several morphometric terminologies associated with the relay ramps are shown in (**D**).

4.2. Mineralogy

Eleven targeted CRISM observations (Figure 6A) were used to infer the mineralogy from the study region (Figure 6B). We identified olivine, pyroxene (high-calcium pyroxene (HCP); low-calcium pyroxene (LCP)), plagioclase (Figure 6B), as well as phyllosilicates, hydrated sulfates, and hydrated silica by analyzing the general waveform of the reflectance spectra of groups of pixels (10 s to 100 s of pixels) within each CRISM observation. We focused on significant absorption bands within the 1.0–2.6 μm interval (Figure 6C). Igneous rock minerals such as HCP and LCP were spectrally identified on the graben floors by absorption at 1 and 2 μm with different absorption centers (LCP: 0.9–1.8 μm, HCP:1.05–2.3 μm) [59,60] due to crystal field transition. Olivine has overlapping absorptions near 0.85, 1.05, and 1.15 μm, and it broadens towards longer wavelengths with increasing Fe content and grain size [60]. Although differences in grain size between separate olivine detections were not identifiable, color differences were apparent, with outcrops appearing as black, dark to light grey, and red (Figure 3B).

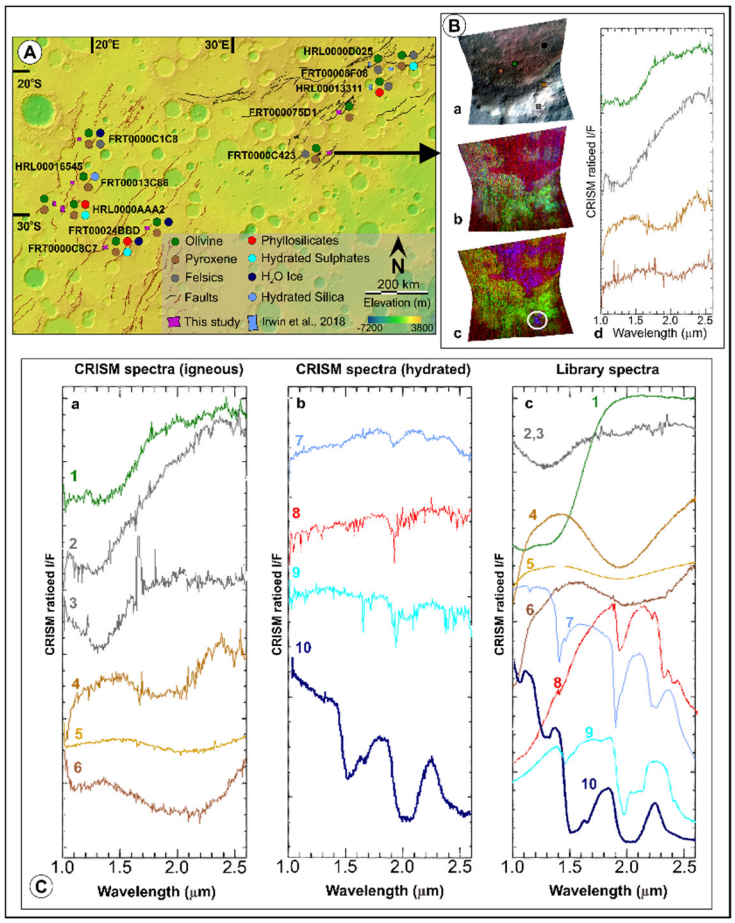

Figure 6. CRISM analysis and minerals detected in the study area. (**A**) Location map. WH and NWH structures are traced in red and black. Colored dots represent specific minerals from each observation. (**B**) A sample presentation of the CRISM analysis from FRT0000C423. (**a**) False color composite with four regions of interest marked by four colored squares which correspond to the colors of the adjacent spectra. The black square represents the location of the neutral spectra used to produce the presented ratioed spectra. (**b**) RGB composite with summary parameters highlighting olivine (red) and pyroxene (green) [R = OLINDEX3 (0.000–0.173), G = LCPINDEX2 (0.000–0.024), B = HCPINDEX2 (0.000–0.027)]. (**c**) RGB composite with summary parameters highlighting olivine (red), pyroxene (green), and plagioclase (blue, outlined by white circle) [R = OLINDEX3 (0.000–0.187), G = LCPINDEX2 (0.000–0.025), B = BD1300 (0.000–0.017)]. (**d**) CRISM-ratioed spectra showing from top to bottom: olivine (green), plagioclase (grey), LCP (light brown), and HCP (dark brown). (**C**) Sample spectra from CRISM observations FRT0000C423, FRT0000C1C8, FRT00013C86, HRL0000AAA2, and FRT0000C8C7. CRISM-ratioed spectra numbered 1–10 and color-coded to match the dot colors used in Figure 1A. (**a**) Spectra are indicative of igneous minerals olivine (1), anorthite (2,3), LCP (4), and HCP (5,6). (**b**) Spectra indicative of hydrated minerals hydrated silica (7), vermiculite (8), and monohydrated sulfate (9), as well as water ice (10). (**c**) Validating USGS library spectra of Fe-olivine (1), anorthite (2,3), LCP augite C1PP48 (4), HCP pyroxene C1S801 (5,6), opal TM8896 (7), vermiculite LAVE01 (8), kieserite F1CC15 (9), water ice (10).

Olivine is the most common mineral, followed by pyroxene. Within one of the more complicated mineralogic sites, observation FRT0000C423, spanning upwards from the graben floor to the horst, olivine was observed at 1.9–2.0 μm, LCP from 2.0 to 2.1 μm, and HCP from 2.1 to 2.3 μm. In most cases, the pyroxene on graben floors is dominated by HCP and sometimes shows no LCP. Two exceptions, however, are in observations FRT0000C8C7 and FRT00024BBD, where the pyroxene is predominately LCP. In another case, observation FRT0000C1C8, the graben floor of mostly olivine surrounds a mixture of HCP and occasionally LCP. Within FRT0000C1C8, a felsic signature was peculiarly found on the rims of two craters on the graben floor, whereas within FRT0000C423, a felsic unit was found within the wall of a graben about 50 m below the plateau surrounded by

HCP and olivine. Our observation is consistent with the observations of Irwin et al. (2018) [41] within the extensional structures of the NWH region, which yielded similar mineralogy. Felsic (silica-rich) rocks are found only in the ejecta or the crater floor, where the basement crust is either excavated or exposed.

4.3. Geochemistry

We selected an area dominated by extensional structures of the WH and NWH region (Figure 7A) for further analysis. The concentration of Ca and K (Figure 7B,C) were selected for the analysis to determine the alkaline characteristics of the rocks. Si and Th (Figure 7D,E) were selected to characterize the basement composition.

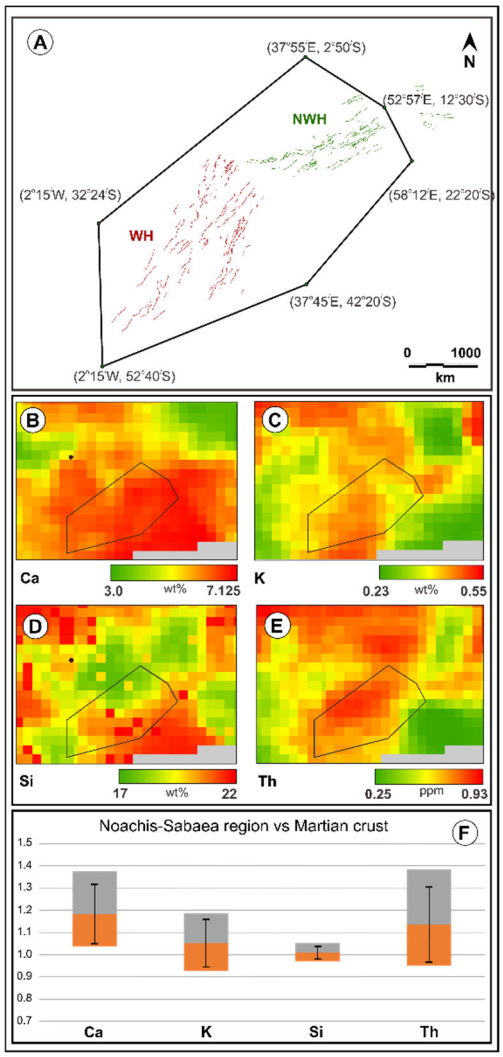

Figure 7. (**A**) Areas with pervasive extensional structures selected for GRS analysis. The coordinates of each corner of the hexagonal area are stated parenthetically. (**B**–**E**) The concentrations of Ca, K, Si, and Th, with the study region outlined (global maps are provided in Supplementary Figures S1 and S2). Mass fractions are percentages except for Th in mg/kg. The study region's geochemistry compared with the rest of the Martian crust, following the modified box plot method. (**F**) The ratios are shown as 25th/75th percentile (orange), 50th/50th percentile, and 75th/25th (grey) percentile [61]. The error bars were calculated by propagating the median average deviations (MAD), where MAD = median (|Xi–median (Xi)|) [62].

Figure 7F shows composition ratios between the study area and the rest of the Martian crust for the elements Ca, K, Si, and Th. Box plots not overlapping with unity identify notable deviations from the two interchangeably and what constitutes the rest of Mars. Error bars show propagated median average deviations. The box plots indicate higher Ca,

K, and Th concentrations than the average Martian composition and Si content is almost equal to the global Martian average.

5. Discussion

Combining the results, we obtain photogeological evidence that the Noachis–Sabaea region sustained extension with progressive deformation. Substantial morphological variations (e.g., unequal graben shoulder heights; suggesting distal side of the basin extending more, basin concentric and basinward dipping normal faults, absence of relay structures; Figure 2A,B) from the CH region to the WH and NWH structures indicate two discrete mechanisms that were responsible for their formation. The origin of the extensional structures in the CH region can be related to the stresses generated during the Hellas basin evolution phase. At that time, Mass Concentration (MASCON)-related basinward drag of the upper lithosphere generated both near and peripheral faults in the surroundings (i.e., the CH structures). Eventually, mantle plume rose. The generation of mantle plumes is often correlated with the large and giant impacts [63] even on Mars [64], where the high thermal impulse of the bolide possibly alters the mantle-core dynamics [65]. Therefore, it is possible to form a mantle plume with a thick diapir that pushes the lithosphere from below.

A similar scenario could have prevailed in our study area because a present-day strong gravity anomaly is observed surrounding the Hellas basin [66,67], which indicates the possibility of the presence of mantle plumes. In the eastern and southern boundary of Hellas, volcanoes from CHVP of the late Noachian age [24] are aligned (Figure 1A) in more or less a similar trend to the extensional structures of the WH region [28]. Although the CHVP is ~3000 km from the extensional structures, their age similarities are intriguing since these might imply genetic links between the CHVP and the extensional features.

A plume-induced continental-type rift hypothesis forming the WH and NWH structures is well-supported by the CRISM data. In similar terrestrial settings, a mantle diapir rose, then decompression melting led to igneous activity where continental rifting occurred [68,69]. In this case, the igneous process was restricted only to fissure-type activities through the faults. HCP and olivine are the two main constituents [70] of such rocks, also consistent with our mineralogic observations. Generally speaking, alkaline rocks contain more alkalis than other silicate rocks, and the excess alkali appears in feldspathoids, sodic pyroxenes, or other alkali-rich phases. The chemical trends observed through GRS are relatable to the alkaline rocks in a tonalite-trondhjemite-granodiorite (TTG) basement (granitic composition) with high Si content in the feldspar [70]. In general, TTG is linked to Archean lithologies on Earth and has been reported from the presumed continental crust of early Mars [71]. Similarly, this part of the southern highlands preserves a crust that is early Noachian in age [15,28,35]. This relatively low K TTG crust was then overlain by the high K basalt resulting in the detection of abundant K in the area. An opposite scenario occurs with the Si and Al content. The primitive crust might have had a higher Si and Al content, but the alkaline rocks associated with the floor basalts (feldspathoids) reduce the total Si and Al content, consistent with the GRS observations.

The basement rocks are covered by flood basalts [18] in arears of lower elevation. In the Earth scenario, at the early stages of continental rifting, flood basalts were very common features [72,73] and were generated by decompression melting of abnormally hot mantle brought by the plumes [74]. Therefore, both signatures are observed here. It should be mentioned that high K does not necessarily imply alkaline rocks (albeit there is a high K subfamily of the alkaline series); calc-alkaline magmatic rocks are also commonly rich in K [75]. The difference is more in the sodium content, for which chemical maps are unavailable. Strictly speaking, the relation between total alkalis vs. silica, among others, serves to distinguish between alkaline and calc-alkaline affinities. Therefore, this is an observation based on the available data. On the other hand, some part of our study area is from continental basements of TTG composition [71,76], which can be chemically

compared with granites or rhyolites. It is also possible that higher K and higher Al related to the calc-alkaline trend is due to the assimilation of crustal granites by basaltic magmas.

6. Possible Scenario

We hypothesize four geologic stages to explain the extensional structures around Hellas basin. We summarize them in chronological order: Initially, a bolide impact (~4 Ga ago) excavates the lithosphere, making the Hellas basin (Stage 1 in Figure 8). The impact generates extensive frictional heat and raises the mantle temperature leading to a density deficit in the surroundings. Hence, MASCON develops. Dragging the pressure gradient from the exterior to the basin interior by visco-elastic flow analogous to lunar counterparts [77] leads to the doming of the mantle (Stage 2 in Figure 8). With time this heated and upraised mantle loses heat by conductive cooling. Eventually, the transient cavity collapses, inducing gravitational collapse. As a result, the surrounding upper lithosphere encompasses a basinward tension (Stage 3 in Figure 8), resulting in extensional structures of the CH region [23]. This process develops unequal scarp heights of the bounding faults and tilted graben floors, as well as normal faults dipping towards the basin interior.

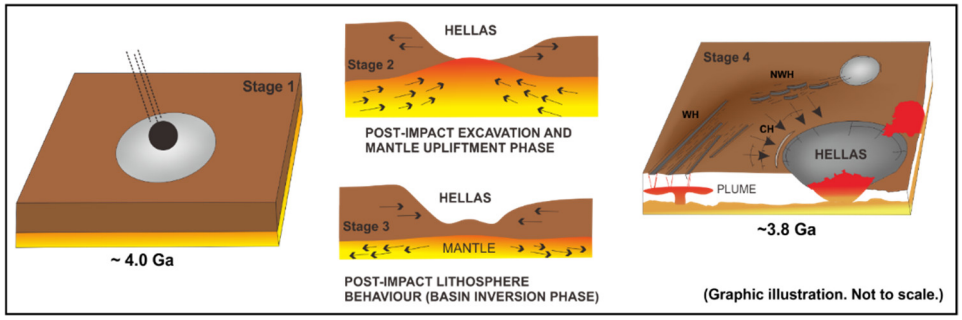

Figure 8. A schematic model explaining the development of the extensional structures. **Stage 1.** A giant impact (~4.0 Ga) excavates the upper crust and penetrates up to the upper mantle. **Stage 2**. Impact-induced frictional heat raises temperatures of the mantle, creating a density deficit relative to the ambient, and it induces a visco-elastic flow, and MASCON develops. **Stage 3**. Due to conductive cooling and viscoelastic evolution, gravitational collapse happens. The collapse drags the upper lithosphere towards the interior of the basin. Consequently, fractures open in the surrounding basin to accommodate the vacant space. **Stage 4**. A mantle plume originates around ~3.8 Ga and initiates rifting.

Subsequently, a mantle plume arises, located just below the (intermediate or relay area between) WH and NWH structures. With two arms radiating from it, this upwelling mantle plume produces a diapir and leads to thermal erosion at the base of the lithosphere. Initially, doming leads to horizontal deviatoric stress that results in crustal stretching, followed by the development of vertical fractures. With continued thermal erosion, the lithospheric mantle triggers uplift and extension (and, therefore, thinning) of the entire lithosphere (including the crust). The fractures act as preferred channels for the ascent of melts extracted from the head of the mantle plume for hot plume material to approach the surface.

7. Conclusions

We evaluated the extensional structures present over a possible diapiric region of the Martian southern highlands and observed a compelling analog to a failed rift zone based on both morphological and compositional characteristics. We detected basalts [18] of alkaline composition which likely resulted from dikes and fractures as surface pathways. The extensional structures are within a similar trend and age resembling those of the CHVP. Therefore, this continental-type rifting (or continental dispersion), mirrors the Rodinia breakup of the continental lithosphere on Earth [78]. We find it plausible that this proto-plate tectonic regime of the lithosphere of the southern highlands of Mars was

triggered by an upwelling mantle plume. This also signifies that Noachian Mars initiated active tectonics due to basal and internal heating, at least in the southern highlands. Similar to the 'heat-pipe' cooling hypothesis [2,6], which is the last significant stage of endogenic resurfacing, a rapid drop in volcanism [79] is observed just after the failed attempt of plate tectonics initiation. Nevertheless, a better understanding of the plume's origin and behavior requires further investigation.

In the future, we would like to conduct a comprehensive set of simulations using the shock physics code iSALE [80,81] covering a wide range of impact conditions mimicking the Hellas impact event. Later, we will use mantle convection codes [82] to understand the impact-induced early Martian mantle behavior. The results may comment on our hypothesis of impact-generated plumes and their possibility to create a proto-plate tectonic scenario.

Supplementary Materials: The following supporting information can be downloaded at: https://www.mdpi.com/article/10.3390/rs14225664/s1, Figure S1: Gamma-Ray Spectrometer derived Calcium (Ca) distribution (A), Potassium (K) distribution (B) on global Mars; Figure S2: Gamma-Ray Spectrometer derived Silica (Si) distribution (A), Thorium (Th) distribution (B) on global Mars; Figure S3: Mafic spectral parameter highlights of three sample CRISM observations within the study area. Minerals highlighted are olivine (red), low-calcium pyroxene (green), and high-calcium pyroxene (blue): (A) CRISM observation FRT00024BBD. False color composite (top). RGB composite with summary parameters [R=OLINDEX (0.000–0.129), G=LCPINDEX2 (0.000–0.031), B= HCPINDEX2 (0.000–0.025)] (middle). HRSC-MOLA blended DEM showing the nearly 2 km relief of the graben wall (bottom). (B) CRISM observation FRT0000C1C8. False color composite (top). RGB composite with summary parameters [R=OLINDEX (0.000–0.109), G=LCPINDEX2 (0.000–0.019), B= HCPINDEX2 (0.000–0.005)] (middle). HRSC/MOLA blended DEM showing the observation's position on the graben floor (bottom). (C) CRISM observation FRT0000C8C7. False color composite (top). RGB composite with summary parameters [R=OLINDEX (0.000–0.081), G=LCPINDEX2 (0.000–0.018), B= HCPINDEX2 (0.000–0.020)] (middle). HRSC-MOLA blended DEM of the southernmost section of the study area where the observation partially covers a south facing graben wall.

Author Contributions: Conceptualization, T.R. and G.K.; Methodology, T.R., G.K. and K.K.; Structural Analysis, T.R.; Mineralogical Analysis, G.S. and T.R.; Geochemical Analysis S.K. and T.R. Formal Analysis, T.R., G.K. and K.K.; Investigation, T.R.; Resources, T.R., G.S. and S.K.; Data Curation, T.R., G.S. and S.K.; Writing–Original Draft Preparation, T.R.; Writing–Review and Editing, T.R., G.K., G.S., S.K. and K.K.; Supervision, G.K. and K.K.; Funding Acquisition, K.K. and G.K. All authors have read and agreed to the published version of the manuscript.

Funding: This work was supported by JSPS KAKENHI Grant Number 18F18312 to TR and KK, and the Italian Ministry for Education, University and Research (MIUR) ex 60% grant to GK. SK was supported by NASA MDAP Grant 80NSSC18K1375. GS is funded by the GeoQuTe Lab (Laboratorio di Geodinamica Quantitativa e Telerilevamento) of Roma Tre University.

Data Availability Statement: Not applicable.

Acknowledgments: We acknowledge Glendon J. Rewerts of LSU for his effort in GRS data analysis. We also thank the constructive comments by the reviewers.

Conflicts of Interest: The authors declare no conflict of interest.

References

1. Schubert, G.; Turcotte, D.L.; Olson, P. *Mantle Convection in the Earth and Planets*; Cambridge University Press: Cambridge, UK, 2001; ISBN 9780521353670.
2. Moore, W.B.; Simon, J.I.; Webb, A.A.G. Heat-Pipe Planets. *Earth Planet. Sci. Lett.* **2017**, *474*, 13–19. https://doi.org/10.1016/j.epsl.2017.06.015.
3. Parro, L.M.; Jiménez-Díaz, A.; Mansilla, F.; Ruiz, J. Present-Day Heat Flow Model of Mars. *Sci. Rep.* **2017**, *7*, 45629. https://doi.org/10.1038/srep45629.
4. Maruyama, S. Plume Tectonics. *J. Geol. Soc. Jpn.* **1994**, *100*, 24–49. https://doi.org/10.5575/geosoc.100.24.
5. Baker, V.R.; Maruyama, S.; Dohm, J.M. Tharsis Superplume and the Geological Evolution of Early Mars. In *Superplumes: Beyond Plate Tectonics*; Springer: Dordrecht, The Netherlands, 2007; pp. 507–522. https://doi.org/10.1007/978-1-4020-5750-2_16.
6. Moore, W.B.; Webb, A.A.G. Heat-Pipe Earth. *Nature* **2013**, *501*, 501–505. https://doi.org/10.1038/nature12473.

7. Acuña, M.H.; Connerney, J.E.P.; Ness, N.F.; Lin, R.P.; Mitchell, D.; Carlson, C.W.; McFadden, J.; Anderson, K.A.; Rème, H.; Mazelle, C.; et al. Global Distribution of Crustal Magnetization Discovered by the Mars Global Surveyor MAG/ER Experiment. *Science* **1999**, *284*, 790–793. https://doi.org/10.1126/science.284.5415.790.
8. Connerney, J.E.P.P.; Acuna, M.H.; Ness, N.F.; Kletetschka, G.; Mitchell, D.L.; Lin, R.P.; Reme, H. Tectonic Implications of Mars Crustal Magnetism. *Proc. Natl. Acad. Sci. USA* **2005**, *102*, 14970–14975. https://doi.org/10.1073/pnas.0507469102.
9. Mittelholz, A.; Johnson, C.L.; Feinberg, J.M.; Langlais, B.; Phillips, R.J. Timing of the Martian Dynamo: New Constraints for a Core Field 4.5 and 3.7 Ga Ago. *Sci. Adv.* **2020**, *6*, eaba0513. https://doi.org/10.1126/SCIADV.ABA0513.
10. Nimmo, F.; Stevenson, D.J. Influence of Early Plate Tectonics on the Thermal Evolution and Magnetic Field of Mars. *J. Geophys. Res. Planets* **2000**, *105*, 11969–11979. https://doi.org/10.1029/1999JE001216.
11. Sleep, N.H. Martian Plate Tectonics. *J. Geophys. Res.* **1994**, *99*, 5639. https://doi.org/10.1029/94JE00216.
12. Hauber, E.; Kronberg, P. Tempe Fossae, Mars: A Planetary Analogon to a Terrestrial Continental Rift? *J. Geophys. Res. E Planets* **2001**, *106*, 20587–20602. https://doi.org/10.1029/2000JE001346.
13. Yin, A. An Episodic Slab-Rollback Model for the Origin of the Tharsis Rise on Mars: Implications for Initiation of Local Plate Subduction and Final Unification of a Kinematically Linked Global Plate-Tectonic Network on Earth. *Lithosphere* **2012**, *4*, 553–593. https://doi.org/10.1130/l195.1.
14. Yin, A. Structural Analysis of the Valles Marineris Fault Zone: Possible Evidence for Large-Scale Strike-Slip Faulting on Mars. *Lithosphere* **2012**, *4*, 286–330. https://doi.org/10.1130/l192.1.
15. Tanaka, K.L.; Robbins, S.J.; Fortezzo, C.M.; Skinner, J.A.; Hare, T.M. The Digital Global Geologic Map of Mars: Chronostratigraphic Ages, Topographic and Crater Morphologic Characteristics, and Updated Resurfacing History. *Planet. Space Sci.* **2014**, *95*, 11–24. https://doi.org/10.1016/j.pss.2013.03.006.
16. Breuer, D.; Spohn, T. Early Plate Tectonics versus Single-Plate Tectonics on Mars: Evidence from Magnetic Field History and Crust Evolution. *J. Geophys. Res.* **2003**, *108*, 5072. https://doi.org/10.1029/2002JE001999.
17. Buczkowski, D.L.; Seelos, K.D.; Cooke, M.L. Giant Polygons and Circular Graben in Western Utopia Basin, Mars: Exploring Possible Formation Mechanisms. *J. Geophys. Res. Planets* **2012**, *117*. https://doi.org/10.1029/2011JE003934.
18. Rogers, A.D.; Nazarian, A.H. Evidence for Noachian Flood Volcanism in Noachis Terra, Mars, and the Possible Role of Hellas Impact Basin Tectonics. *J. Geophys. Res. E Planets* **2013**, *118*, 1094–1113. https://doi.org/10.1002/jgre.20083.
19. Williams, D.A.; Greeley, R.; Manfredi, L.; Raitala, J.; Neukum, G. The Circum-Hellas Volcanic Province, Mars: Assessment of Wrinkle-Ridged Plains. *Earth Planet. Sci. Lett.* **2010**, *294*, 492–505. https://doi.org/10.1016/j.epsl.2009.10.007.
20. Luzzi, E.; Rossi, A.P.; Carli, C.; Altieri, F. Tectono-Magmatic, Sedimentary, and Hydrothermal History of Arsinoes and Pyrrhae Chaos, Mars. *J. Geophys. Res. Planets* **2020**, *125*, e2019JE006341. https://doi.org/10.1029/2019JE006341.
21. De, K.; Ruj, T.; Kundu, A.; Dasgupta, N.; Kawai, K. Evolution of Pyrrhae Fossae, Mars: An Explication from the Age Estimation Using the Buffered Crater Counting Technique. *Curr. Sci.* **2021**, *121*, 906. https://doi.org/10.18520/cs/v121/i7/906-911.
22. Andrews-Hanna, J.C. The Formation of Valles Marineris: 2. Stress Focusing along the Buried Dichotomy Boundary. *J. Geophys. Res. Planets* **2012**, *117*. https://doi.org/10.1029/2011JE003954.
23. Wichman, R.W.; Schultz, P.H. Sequence and Mechanisms of Deformation around the Hellas and Isidis Impact Basins on Mars. *J. Geophys. Res.* **1989**, *94*, 17333. https://doi.org/10.1029/JB094iB12p17333.
24. Williams, D.A.; Greeley, R.; Fergason, R.L.; Kuzmin, R.; McCord, T.B.; Combe, J.-P.; Head, J.W.; Xiao, L.; Manfredi, L.; Poulet, F.; et al. The Circum-Hellas Volcanic Province, Mars: Overview. *Planet. Space Sci.* **2009**, *57*, 895–916. https://doi.org/10.1016/j.pss.2008.08.010.
25. Ruj, T.; Komatsu, G.; Dohm, J.M.; Miyamoto, H.; Salese, F. Generic Identification and Classification of Morphostructures in the Noachis-Sabaea Region, Southern Highlands of Mars. *J. Maps* **2017**, *13*, 755–766. https://doi.org/10.1080/17445647.2017.1379913.
26. Golombek, M.P.; Phillips, R.J. Mars Tectonics. In *Planetary Tectonics*; Cambridge University Press: Cambridge, UK, 2009; pp. 183–232.
27. Allemand, P.; Thomas, P. Small-Scale Models of Multiring Basins. *J. Geophys. Res. Planets* **1999**, *104*, 16501–16514. https://doi.org/10.1029/1999JE900008.
28. Ruj, T.; Komatsu, G.; Pasckert, J.H.; Dohm, J.M. Timings of Early Crustal Activity in Southern Highlands of Mars: Periods of Crustal Stretching and Shortening. *Geosci. Front.* **2019**, *10*, 1029–1037. https://doi.org/10.1016/j.gsf.2018.05.016.
29. Malin, M.C.; Bell, J.F.; Cantor, B.A.; Caplinger, M.A.; Calvin, W.M.; Clancy, R.T.; Edgett, K.S.; Edwards, L.; Haberle, R.M.; James, P.B.; et al. Context Camera Investigation on Board the Mars Reconnaissance Orbiter. *J. Geophys. Res.* **2007**, *112*, E05S04. https://doi.org/10.1029/2006JE002808.
30. Neukum, G.; Jaumann, R. HRSC: The High Resolution Stereo Camera of Mars Express. *Eur. Sp. Agency Special Publ. ESA SP* **2004**, *1240*, 17–35.
31. Jaumann, R.; Neukum, G.; Behnke, T.; Duxbury, T.C.; Eichentopf, K.; Flohrer, J.; Gasselt, S.; Giese, B.; Gwinner, K.; Hauber, E.; et al. The High-Resolution Stereo Camera (HRSC) Experiment on Mars Express: Instrument Aspects and Experiment Conduct from Interplanetary Cruise through the Nominal Mission. *Planet. Space Sci.* **2007**, *55*, 928–952. https://doi.org/10.1016/j.pss.2006.12.003.
32. Murchie, S.L.; Arvidson, R.; Bedini, P.; Beisser, K.; Bibring, J.-P.; Bishop, J.; Boldt, J.; Cavender, P.; Choo, T.; Clancy, R.T.; et al. Compact Reconnaissance Imaging Spectrometer for Mars (CRISM) on Mars Reconnaissance Orbiter (MRO). *J. Geophys. Res.* **2007**, *112*, E05S03. https://doi.org/10.1029/2006JE002682.

33. Boynton, W.V.; Feldman, W.C.; Mitrofanov, I.G.; Evans, L.G.; Reedy, R.C.; Squyres, S.W.; Starr, R.; Trombka, J.I.; d'Uston, C.; Arnold, J.R.; et al. The Mars Odyssey Gamma-Ray Spectrometer Instrument Suite. *Space Sci. Rev.* **2004**, *110*, 37–83. https://doi.org/10.1023/b:spac.0000021007.76126.15.
34. Rodriguez, J.A.P.; Dobrea, E.N.; Kargel, J.S.; Baker, V.R.; Crown, D.A.; Webster, K.D.; Berman, D.C.; Wilhelm, M.B.; Buckner, D. The Oldest Highlands of Mars May Be Massive Dust Fallout Deposits. *Sci. Rep.* **2020**, *10*, 10347. https://doi.org/10.1038/s41598-020-64676-z.
35. Platz, T.; Michael, G.; Tanaka, K.L.; Skinner, J.A.; Fortezzo, C.M. Crater-Based Dating of Geological Units on Mars: Methods and Application for the New Global Geological Map. *Icarus* **2013**, *225*, 806–827. https://doi.org/10.1016/j.icarus.2013.04.021.
36. Head, J.W.; Wilson, L.; Dickson, J.; Neukum, G. The Huygens-Hellas Giant Dike System on Mars: Implications for Late Noachian-Early Hesperian Volcanic Resurfacing and Climatic Evolution. *Geology* **2006**, *34*, 285–288. https://doi.org/10.1130/G22163.1.
37. Ruj, T.; Komatsu, G.; Pondrelli, M.; Di Pietro, I.; Pozzobon, R. Morphometric Analysis of a Hesperian Aged Martian Lobate Scarp Using High-Resolution Data. *J. Struct. Geol.* **2018**, *113*, 1–9. https://doi.org/10.1016/j.jsg.2018.04.018.
38. Mangold, N.; Allemand, P.; Thomas, P.G.; Vidal, G. Chronology of Compressional Deformation on Mars: Evidence for a Single and Global Origin. *Planet. Space Sci.* **2000**, *48*, 1201–1211. https://doi.org/10.1016/S0032-0633(00)00104-5.
39. Ruj, T.; Kawai, K. A Global Investigation of Wrinkle Ridge Formation Events; Implications towards the Thermal Evolution of Mars. *Icarus* **2021**, *369*, 114625. https://doi.org/10.1016/j.icarus.2021.114625.
40. Andrews-Hanna, J.C.; Zuber, M.T.; Hauck, S.A. Strike-Slip Faults on Mars: Observations and Implications for Global Tectonics and Geodynamics. *J. Geophys. Res.* **2008**, *113*, E08002. https://doi.org/10.1029/2007JE002980.
41. Irwin, R.P.; Wray, J.J.; Mest, S.C.; Maxwell, T.A. Wind-Eroded Crater Floors and Intercrater Plains, Terra Sabaea, Mars. *J. Geophys. Res. Planets* **2018**, *123*, 445–467. https://doi.org/10.1002/2017JE005270.
42. Bandfield, J.L.; Amador, E.S.; Thomas, N.H. Extensive Hydrated Silica Materials in Western Hellas Basin, Mars. *Icarus* **2013**, *226*, 1489–1498. https://doi.org/10.1016/J.ICARUS.2013.08.005.
43. Carter, J.; Poulet, F.; Bibring, J.P.; Mangold, N.; Murchie, S. Hydrous Minerals on Mars as Seen by the CRISM and OMEGA Imaging Spectrometers: Updated Global View. *J. Geophys. Res. Planets* **2013**, *118*, 831–858. https://doi.org/10.1029/2012JE004145.
44. Salese, F.; Di Achille, G.; Neesemann, A.; Ori, G.G.; Hauber, E. Hydrological and Sedimentary Analyses of Well-Preserved Paleofluvial-Paleolacustrine Systems at Moa Valles, Mars. *J. Geophys. Res. Planets* **2016**, *121*, 194–232. https://doi.org/10.1002/2015JE004891.
45. Rogers, A.D.; Hamilton, V.E. Compositional Provinces of Mars from Statistical Analyses of TES, GRS, OMEGA and CRISM Data. *J. Geophys. Res. Planets* **2015**, *120*, 62–91. https://doi.org/10.1002/2014JE004690.
46. Korteniemi, J.; Kukkonen, S. Volcanic Structures Within Niger and Dao Valles, Mars, and Implications for Outflow Channel Evolution and Hellas Basin Rim Development. *Geophys. Res. Lett.* **2018**, *45*, 2934–2944. https://doi.org/10.1002/2018GL077067.
47. Fergason, R.L.; Hare, T.M.; Laura, J. HRSC and MOLA Blended Digital Elevation Model at 200 M. In *Proceedings of the Astrogeology PDS Annex*; US Geological Survey: Flagstaff, AZ, USA, 2018.
48. Bishop, J. Reflectance Spectroscopy of Ferric Sulfate-Bearing Montmorillonites as Mars Soil Analog Materials. *Icarus* **1995**, *117*, 101–119. https://doi.org/10.1006/icar.1995.1145.
49. Flahaut, J.; Carter, J.; Poulet, F.; Bibring, J.P.; van Westrenen, W.; Davies, G.R.; Murchie, S.L. Embedded Clays and Sulfates in Meridiani Planum, Mars. *Icarus* **2015**, *248*, 269–288. https://doi.org/10.1016/j.icarus.2014.10.046.
50. Schmidt, G.; Luzzi, E.; Rossi, A.P.; Pondrelli, M.; Apuzzo, A.; Salvini, F. Protracted Hydrogeological Activity in Arabia Terra, Mars: Evidence from the Structure and Mineralogy of the Layered Deposits of Becquerel Crater. *J. Geophys. Res. Planets* **2022**, *127*, e2022JE007320. https://doi.org/10.1029/2022JE007320.
51. Viviano-Beck, C.E.; Seelos, F.P.; Murchie, S.L.; Kahn, E.G.; Seelos, K.D.; Taylor, H.W.; Taylor, K.; Ehlmann, B.L.; Wisemann, S.M.; Mustard, J.F.; et al. Revised CRISM Spectral Parameters and Summary Products Based on the Currently Detected Mineral Diversity on Mars. *J. Geophys. Res. E Planets* **2014**, *119*, 1403–1431. https://doi.org/10.1002/2014JE004627.
52. Clark, R.N.; King, T.V.V.; Klejwa, M.; Swayze, G.A.; Vergo, N. High Spectral Resolution Reflectance Spectroscopy of Minerals. *J. Geophys. Res.* **1990**, *95*, 12653. https://doi.org/10.1029/JB095iB08p12653.
53. Pelkey, S.M.; Mustard, J.F.; Murchie, S.; Clancy, R.T.; Wolff, M.; Smith, M.; Milliken, R.E.; Bibring, J.P.; Gendrin, A.; Poulet, F.; et al. CRISM Multispectral Summary Products: Parameterizing Mineral Diversity on Mars from Reflectance. *J. Geophys. Res. Planets* **2007**, *112*, 8–14. https://doi.org/10.1029/2006JE002831.
54. Rani, A.; Basu Sarbadhikari, A.; Hood, D.R.; Gasnault, O.; Nambiar, S.; Karunatillake, S. Consolidated Chemical Provinces on Mars: Implications for Geologic Interpretations. *Geophys. Res. Lett.* **2022**, *49*, e2022GL099235. https://doi.org/10.1029/2022GL099235.
55. Ojha, L.; Karunatillake, S.; Karimi, S.; Buffo, J. Amagmatic Hydrothermal Systems on Mars from Radiogenic Heat. *Nat. Commun.* **2021**, *12*, 1754. https://doi.org/10.1038/s41467-021-21762-8.
56. Fossen, H.; Rotevatn, A. Fault Linkage and Relay Structures in Extensional Settings—A Review. *Earth-Science Rev.* **2016**, *154*, 14–28. https://doi.org/10.1016/j.earscirev.2015.11.014.
57. Acocella, V.; Morvillo, P.; Funiciello, R. What Controls Relay Ramps and Transfer Faults within Rift Zones? Insights from Analogue Models. *J. Struct. Geol.* **2005**, *27*, 397–408. https://doi.org/10.1016/j.jsg.2004.11.006.
58. Pagli, C.; Yun, S.-H.; Ebinger, C.; Keir, D.; Wang, H. Strike-Slip Tectonics during Rift Linkage. *Geology* **2019**, *47*, 31–34. https://doi.org/10.1130/G45345.1.

59. Skok, J.R.; Mustard, J.F.; Tornabene, L.L.; Pan, C.; Rogers, D.; Murchie, S.L. A Spectroscopic Analysis of Martian Crater Central Peaks: Formation of the Ancient Crust. *J. Geophys. Res. E Planets* **2012**, *117*. https://doi.org/10.1029/2012JE004148.
60. Viviano, C.E.; Murchie, S.L.; Daubar, I.J.; Morgan, M.F.; Seelos, F.P.; Plescia, J.B. Composition of Amazonian Volcanic Materials in Tharsis and Elysium, Mars, from MRO/CRISM Reflectance Spectra. *Icarus* **2019**, *328*, 274–286. https://doi.org/10.1016/j.icarus.2019.03.001.
61. Karunatillake, S.; Squyres, S.W.; Gasnault, O.; Keller, J.M.; Janes, D.M.; Boynton, W.V.; Finch, M.J. Recipes for Spatial Statistics with Global Datasets: A Martian Case Study. *J. Sci. Comput.* **2011**, *46*, 439–451. https://doi.org/10.1007/s10915-010-9412-z.
62. Susko, D.; Karunatillake, S.; Kodikara, G.; Skok, J.R.; Wray, J.; Heldmann, J.; Cousin, A.; Judice, T. A Record of Igneous Evolution in Elysium, a Major Martian Volcanic Province. *Sci. Rep.* **2017**, *7*, 43177. https://doi.org/10.1038/srep43177.
63. Abbott, D.H.; Isley, A.E. Extraterrestrial Influences on Mantle Plume Activity. *Earth Planet. Sci. Lett.* **2002**, *205*, 53–62. https://doi.org/10.1016/S0012-821X(02)01013-0.
64. Reese, C.C.; Solomatov, V.S.; Baumgardner, J.R.; Stegman, D.R.; Vezolainen, A.V. Magmatic Evolution of Impact-Induced Martian Mantle Plumes and the Origin of Tharsis. *J. Geophys. Res. E Planets* **2004**, *109*, E08009. https://doi.org/10.1029/2003JE002222.
65. Roberts, J.H.; Barnouin, O.S. The Effect of the Caloris Impact on the Mantle Dynamics and Volcanism of Mercury. *J. Geophys. Res. E Planets* **2012**, *117*, 1–15. https://doi.org/10.1029/2011JE003876.
66. Zuber, M.T.; Solomon, S.C.; Phillips, R.J.; Smith, D.E.; Tyler, G.L.; Aharonson, O.; Balmino, G.; Banerdt, W.B.; Head, J.W.; Johnson, C.L.; et al. Internal Structure and Early Thermal Evolution of Mars from Mars Global Surveyor Topography and Gravity. *Science* **2000**, *287*, 1788–1793. https://doi.org/10.1126/science.287.5459.1788.
67. Genova, A.; Goossens, S.; Lemoine, F.G.; Mazarico, E.; Neumann, G.A.; Smith, D.E.; Zuber, M.T. Seasonal and Static Gravity Field of Mars from MGS, Mars Odyssey and MRO Radio Science. *Icarus* **2016**, *272*, 228–245. https://doi.org/10.1016/j.icarus.2016.02.050.
68. Keen, C.E.; Courtney, R.C.; Dehler, S.A.; Williamson, M.C. Decompression Melting at Rifted Margins: Comparison of Model Predictions with the Distribution of Igneous Rocks on the Eastern Canadian Margin. *Earth Planet. Sci. Lett.* **1994**, *121*, 403–416. https://doi.org/10.1016/0012-821X(94)90080-9.
69. Chorowicz, J. The East African Rift System. *J. African Earth Sci.* **2005**, *43*, 379–410. https://doi.org/10.1016/J.JAFREARSCI.2005.07.019.
70. Philpotts, A.; Ague, J. *Principles of Igneous and Metamorphic Petrology*; Cambridge University Press: Cambridge, UK, 2009; ISBN 9780521880060.
71. Sautter, V.; Toplis, M.J.; Wiens, R.C.; Cousin, A.; Fabre, C.; Gasnault, O.; Maurice, S.; Forni, O.; Lasue, J.; Ollila, A.; et al. In Situ Evidence for Continental Crust on Early Mars. *Nat. Geosci.* **2015**, *8*, 605–609. https://doi.org/10.1038/ngeo2474.
72. Jackson, I. *The Earth's Mantle; Composition, Structure, and Evolution*; Jackson, I., Ed.; Cambridge University Press: Cambridge, UK, 1998; ISBN 9780511573101.
73. Courtillot, V.; Jaupart, C.; Manighetti, I.; Tapponnier, P.; Besse, J. On Causal Links between Flood Basalts and Continental Breakup. *Earth Planet. Sci. Lett.* **1999**, *166*, 177–195. https://doi.org/10.1016/S0012-821X(98)00282-9.
74. White, R.S.; McKenzie, D. Mantle Plumes and Flood Basalts. *J. Geophys. Res.* **1995**, *100*, 17543–17585. https://doi.org/10.1029/95jb01585.
75. Roberts, M.P.; Clemens, J.D. Origin of High-Potassium, Talc-Alkaline, I-Type Granitoids. *Geology* **1993**, *21*, 825. https://doi.org/10.1130/0091-7613(1993)021<0825:OOHPTA>2.3.CO;2.
76. Sautter, V.; Toplis, M.J.; Beck, P.; Mangold, N.; Wiens, R.; Pinet, P.; Cousin, A.; Maurice, S.; LeDeit, L.; Hewins, R.; et al. Magmatic Complexity on Early Mars as Seen through a Combination of Orbital, in-Situ and Meteorite Data. *Lithos* **2016**, *254–255*, 36–52. https://doi.org/10.1016/J.LITHOS.2016.02.023.
77. Melosh, H.J.; Freed, A.M.; Johnson, B.C.; Blair, D.M.; Andrews-Hanna, J.C.; Neumann, G.A.; Phillips, R.J.; Smith, D.E.; Solomon, S.C.; Wieczorek, M.A.; et al. The Origin of Lunar Mascon Basins. *Science* **2013**, *340*, 1552–1555. https://doi.org/10.1126/science.1235768.
78. Li, Z.X.; Li, X.H.; Kinny, P.D.; Wang, J.; Zhang, S.; Zhou, H. Geochronology of Neoproterozoic Syn-Rift Magmatism in the Yangtze Craton, South China and Correlations with Other Continents: Evidence for a Mantle Superplume That Broke up Rodinia. *Precambrian Res.* **2003**, *122*, 85–109. https://doi.org/10.1016/S0301-9268(02)00208-5.
79. Carr, M.H.; Head, J.W. Geologic History of Mars. *Earth Planet. Sci. Lett.* **2010**, *294*, 185–203. https://doi.org/10.1016/j.epsl.2009.06.042.
80. Wünnemann, K.; Collins, G.S.; Melosh, H.J. A Strain-Based Porosity Model for Use in Hydrocode Simulations of Impacts and Implications for Transient Crater Growth in Porous Targets. *Icarus* **2006**, *180*, 514–527. https://doi.org/10.1016/J.ICARUS.2005.10.013.
81. Collins, G.S.; Melosh, H.J.; Ivanov, B.A. Modeling Damage and Deformation in Impact Simulations. *Meteorit. Planet. Sci.* **2004**, *39*, 217–231. https://doi.org/10.1111/J.1945-5100.2004.TB00337.X.
82. Kameyama, M. ACuTEMan: A Multigrid-Based Mantle Convection Simulation Code and Its Optimization to the Earth Simulator. *J. Earth Simulator* **2005**, *4*, 2–10.